INTERNATIONAL JOURNAL OF REFRIGERATION 82 (2017) 529–540

Available online at www.sciencedirect.com

ScienceDirect

journal homepage: www.elsevier.com/locate/ijrefrig

Development of a switchless sorption compressor for the cryogenic refrigeration within the METIS instrument: Part II. Experimental demonstration

Y. Wu [a,b,*], C.H. Vermeer [c], H.J. Holland [b], B. Benthem [d], H.J.M. ter Brake [b]

[a] Institute of Process Equipment, Zhejiang University, Zheda Rd. 38, 310027, Hangzhou, China
[b] Faculty of Science & Technology, University of Twente, Drienerlolaan 5, 7522NB, Enschede, The Netherlands
[c] SuperACT, Marterstraat 66, 7559AJ Hengelo, The Netherlands
[d] Airbus Defence and Space Netherlands B.V., P.O. Box 32070, 2303DB, Leiden, The Netherlands

ARTICLE INFO

Article history:
Available online 27 June 2017

Keywords:
Sorption compressor
Cryogenics
Cryogenic refrigeration
Heat switch
E-ELT
METIS

ABSTRACT

Due to its vibration-free feature, sorption-based refrigeration technology has been proposed for the cryogenic cooling of the Mid-infrared E-ELT Imager and Spectrograph (METIS) instrument in the European Extremely Large Telescope. Sorption compressor is the most critical component in the METIS sorption refrigerator. A switchless sorption compressor has been designed for replacing the conventional gas-gap heat switch design. In this paper, the METIS switchless sorption compressor is validated in an experimental setup with a down-scaled version. The detailed design of the sorption compressor is introduced and the experimental setup is described. Then, the experimental procedures and results are discussed, including single-cell operation, multi-cell operation, and verification of the effects of the aluminum-foil inserts, the cycle time and the heat-sink temperature on the compressor performance. Finally, the experimental result showed good agreement with the simulations, and the deviation from the simulation to the measurement is caused by the model input inaccuracy.

Développement d'un compresseur à sorption sans interrupteur pour le froid cryogénique des instrument METIS Partie II : Démonstration expérimentale

Mots clés : Compresseur à sorption ; Cryogénie ; Froid cryogénique ; Interrupteur thermique ; E-ELT (Télescope géant européen) ; METIS

* *Corresponding author.* Institute of Process Equipment, Zhejiang University, Zheda Rd. 38, 310027, Hangzhou, China.
E-mail address: yzwu@zju.edu.cn (Y. Wu).

http://dx.doi.org/10.1016/j.ijrefrig.2017.06.023

Nomenclature

Abbreviations

bara	Absolute pressure unit, bar
barg	Gauge pressure unit, bar
BSC	The baseline cells
BSL	Best straight line
CFHX	Counter flow heat exchanger
E-ELT	European Extremely Large Telescope
FEM	Finite element method
FS	Full scale
GGHS	Gas-gap heat switch
GM	Gifford-McMahon
JT	Joule-Thomson
LN2	Liquid nitrogen
METIS	The Mid-infrared E-ELT Imager and Spectrograph
RCEC	The radial-conductance-enhanced cells
Rd	Read value of a measurement

Symbols

C	Scaling parameter for regulating the mass flow rate [kg s^{-1} Pa^{-1}]
$c_{p,sor}$	Heat capacity of the sorbent [J kg^{-1} K^{-1}]
D_{sor}	Diameter of the sorbent [m]
$k_{eff,sor}$	Effective thermal conductivity of the sorbent [W m^{-1} K^{-1}]
L_{cell}	Length of the sorption compressor cell [m]
$\dot{m}$	Mass flow rate [kg s^{-1}]
Δm	Mass transferred per cycle [kg]
P_{avg}	Average input power [W]
P_{HT}	Heating power [W]
p_{cell}	Pressure in the sorption compressor cell [Pa]
p_h	High pressure of the sorption compression cycle [Pa]
p_l	Low pressure of the sorption compression cycle [Pa]
T_{HS}	Heat-sink temperature [K]
t_{cyc}	Cycle time [s]
t_H	Heating time [s]
x_{ads}	Normalized adsorption amount of the working fluid [kg kg^{-1}]

1. Introduction

As one of the scientific instruments on the European Extremely Large Telescope (E-ELT), METIS (the Mid-infrared E-ELT Imager and Spectrograph) requires cryogenic refrigeration at multiple temperature levels to enable its cold optics and infrared detectors working functionally (Brandl et al., 2010). University of Twente proposed a vibration-free refrigeration technology based on the sorption Joule–Thomson (JT) refrigerator to serve such sensitive device. A series of developments has been carried out to demonstrate the feasibility and technical readiness of such cooling method.

In the early stage, a baseline design of the METIS refrigerator chain was conducted (Wu et al., 2017c) based on the cooling specification provided by the METIS designer. In this conceptual design, the refrigerator system is composed of three sorption JT refrigerator stages cascaded via thermal links. By using neon, hydrogen and helium as the working fluids respectively, those refrigerator stages are responsible for providing cooling powers of 1.4 W at 40 K, 1.1 W at 25 K and 0.4 W at 8 K, respectively. Thermally sunk at 70 K, the sorption compressors of the METIS refrigerator chain are of great concern according to the baseline design, as they contribute the most to the inefficiency and size (as well as mass) of the system. Therefore, studying, designing and demonstrating the sorption compressor are critical in the development of the METIS refrigerator.

A one-dimensional dynamic model for the sorption compressor was developed to simulate the heat and mass transfer within the compressor cell during the operation and to evaluate the performance of the cell (Wu et al., 2017a). By using this model, an improved, switchless sorption-compressor design has been investigated and finally accepted for the METIS compressor (Wu et al., 2017b). The switchless configuration is easy to manufacture and assemble and consequently has a low cost. It is more suitable for large scale ground application, such as METIS refrigerator, whereas the original design associated with the gas-gap heat switch (GGHS) is better for the space-borne mission. Based on such a switchless design, the dimensions of the sorption compressor-cell for the METIS refrigerator has been optimized and determined.

Furthermore, analyses have been done for improving the cell performance by reducing the radial temperature gradient in the carbon. The results indicate that the helium compressor cell can gain 24% more mass flow by adding aluminum foils between the carbon pills without degrading the efficiency (Mulder, 2014). However, this concept has not been experimentally verified. In this paper, we present the experimental demonstration of the METIS sorption compressor. The helium sorption compressor was finally chosen for an experimental demonstration, as it consumes more than 50% of the total input power and requires about 59% cells among all the cells for the entire refrigerator (Wu et al., 2017c). According to the optimization results obtained in the previous study [4], the sorption-compressor cell was designed, fabricated and assembled as described in Sec. 2. Two types of cell were made: the baseline cells (BSC) with no aluminum foils between the carbon pills, and the radial-conductance-enhanced cells (RCEC) in which aluminum foils are placed between the carbon pills. We also designed and built an experimental setup for operating and measuring these helium sorption-compressor cells, which is presented in Sec. 3. Sec. 4 discussed the experimental procedures and results, including the introductory tests, single-cell operation, multi-cell operation, and verification of the effects of the aluminum foil inserts, the cycle time and the heat-sink temperature on the performance of the compressor. Finally, the paper is closed with conclusions.

2. Switchless sorption compressor cell

Fig. 1 is a drawing of the switchless sorption-compressor cell that presents the detailed design. The cell dimensions followed

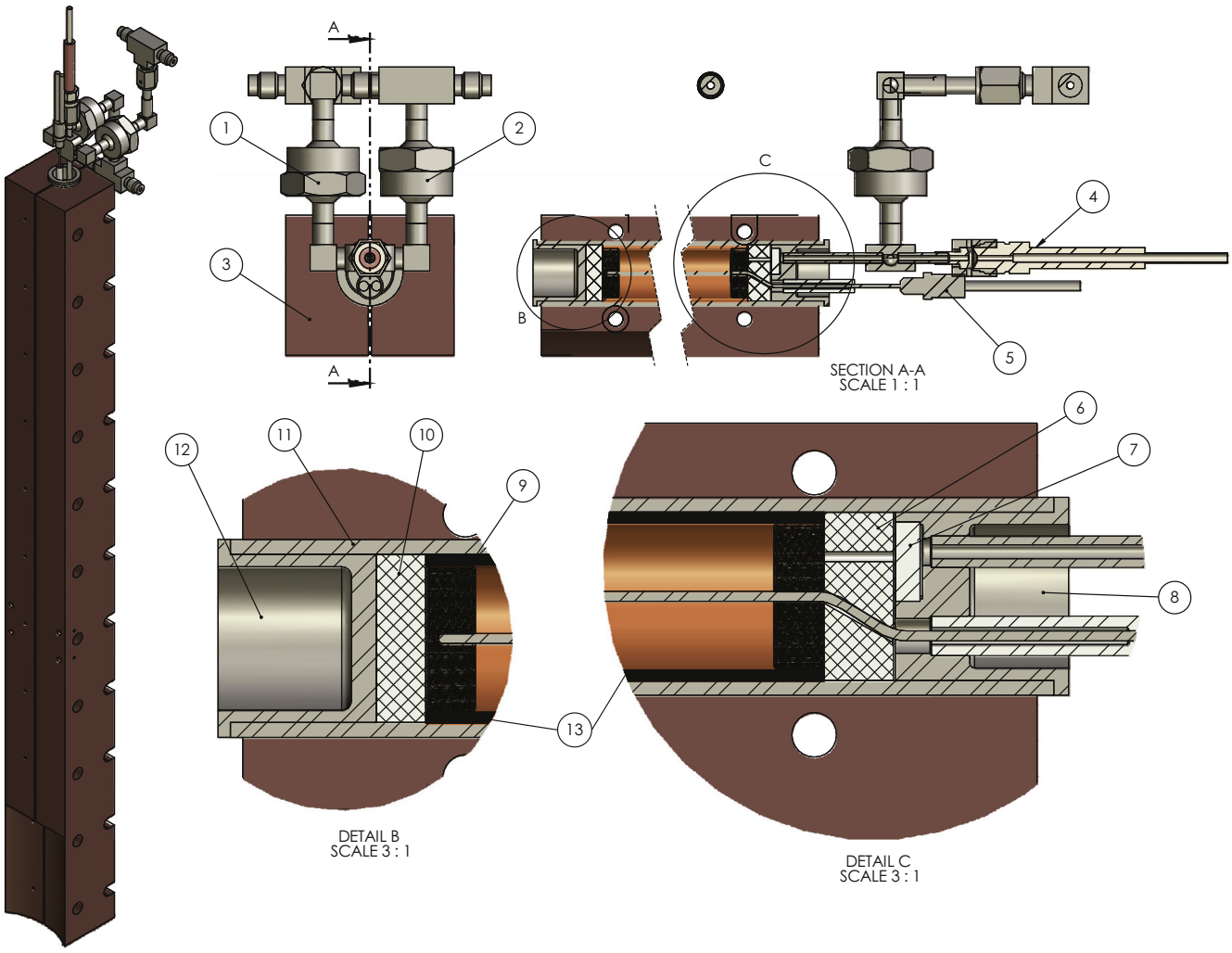

Fig. 1 – Detailed design of the helium sorption-compressor cell: 1 & 2. Check valves; 3. Heat-sink copper block; 4. Soft copper pinch-off; 5. Heater; 6 & 10. Teflon pills for insulating the ends; 7. Filter; 8 & 12. End caps of the container; 9. Carbon pill (only the first and the last pill are shown in the figure); 11. Container wall; 13. Kapton insulation layer.

the optimization results presented in the previous paper, except for the thickness of the container wall that is much thicker (1.5 mm instead of 0.25 mm). Using a thicker wall will not degrade the helium compressor performance too much because the temperature swing and gradient in the container wall will be very limited compared to that in the carbon and the insulation layer. On the other hand, this thicker wall allows us also to operate the cells with neon for test purposes if need at very high pressures (up to 90 bar). The cell container was sealed by a blind cap (the cap in detail B) at one side (blind side) and a similar cap (the cap in detail C) with the sealed heater and check valves set at the other side (open side). The end caps were designed not just for standing high pressure but also for orbital welding. FEM thermal analysis was performed to optimize the cap dimensions such that parts in the container are not burned during the welding process.

The adsorbent material is saran carbon. It has a porosity of 50% and was shaped into cylindrical pills with a height of 5.08 mm and a diameter of 14.5 mm. A central hole of 1.15 mm was drilled for the heater. The space for the carbon in the container is 505 mm long. The radial-conductance-enhanced cells (RCEC) were made by inserting thin aluminum foils between the carbon pills. The aluminum foils are 40 m thick and have a diameter of 12 mm. Thus, 98 carbon pills were loaded into the RCEC, while the baseline cells (BSC) contain 99 pills.

The insulation layer between the carbon and the container wall was made by wrapping Kapton foil (500FN131, thickness of 127 μm) into an annulus cylinder. The cryogenic shrinkage of the insulation layer will be about 3.8% (data for Polyamide from Marquardt et al., 2001) which is taken into account in the parasitic volume and corrected for in the numerical simulation by using the one-dimensional dynamic model (Wu et al., 2017a). The gas channels created by the Kapton shrinkage are negligibly small. However, the triangular channel formed between the Kapton film edge and the carbon pills in the axial direction, with an approximate hydraulic diameter of the film thickness, naturally becomes the channel for the working fluid flowing in and out. The thermal insulation between cell and heat sink at the ends of the cell was

established by two Teflon pills (details B and C in Fig. 1). A sintered stainless steel filter with media grade 100 µm and a thickness of 0.1 inch (Mott 1100-4-4-0.1-100) was placed between the Teflon pill and the gas tube connection to the check valves to prevent any carbon particles from flowing into the JT cold stage which could cause clogging (part 7 in detail C).

Check valves play an important role (Wiegerinck et al., 2006; Burger et al., 2007) in transforming the periodic pressure swing inside the sorption-compressor cell into a more or less continuous flow that drives the JT cold stage. A check valve requires low void volume, low leak rate, low pressure drop in forward direction and low cracking pressure to keep the sorption refrigerator working properly and efficiently. In current study, a Swagelok check valve (6LV-CW4BW6M-NE) with a neoprene sealing material at the valve poppet was selected after qualification tests at 77 K.

3. Experimental setup

The experimental setup for operating and measuring the helium sorption-compressor cells is designed not just for verifying the theoretical design of the switchless sorption compressor but also for demonstrating the feasibility of the compressor for the METIS refrigerator. More than 40 cells are used for the METIS refrigerator. However, the parallel operation of these cells allows us to verify the design and performance in a down-scaled version using only a limited number of cells. Therefore, the setup was designed for four full-size helium compressor cells, expected to deliver about 8.89% of the total mass flow rate required for the METIS helium stage.

Fig. 2 presents a schematic layout of the down-scaled helium sorption compressor setup. The manufacturing of the sorption-compressor cells was started with six cells (numbers 1–6), and four of these (Cells 1, 3, 4 and 5) were selected and mounted in the setup in parallel. Cells 1 and 3 are BSC, whereas Cells 4 and 5 are RCEC.

The 70 K heat sink in this setup is provided by a GM cooler, and the heat-sink assembly is shown in Fig. 3. The cylindrical cell is tightly clamped by two thick copper blocks for distributing the cold heat-sinking as uniformly as possible. The four copper-clamped cells stand vertically on the 1st stage of the GM cooler with a good thermal contact at the bottom. Furthermore, thermal links are planned between the middle part of the copper blocks and the 2nd stage of the GM cooler. An FEM thermal analysis was performed to find an optimum thermal anchor point on the copper blocks. The analysis result also confirms that the temperature difference along copper block is 1.05 K and the temperature instability is less than 0.2 K, which are acceptable for the experiment.

2.0 L and 0.5 L for the high and low-pressure buffers were chosen based on the dynamic performance of the sorption cells and parasitic volumes of the setup. Buffers were used to smoothen the pulsed out-flow generated by the compressor cells and to provide a massive volume that reduces the system storage pressure at the room temperature. The buffers, as well

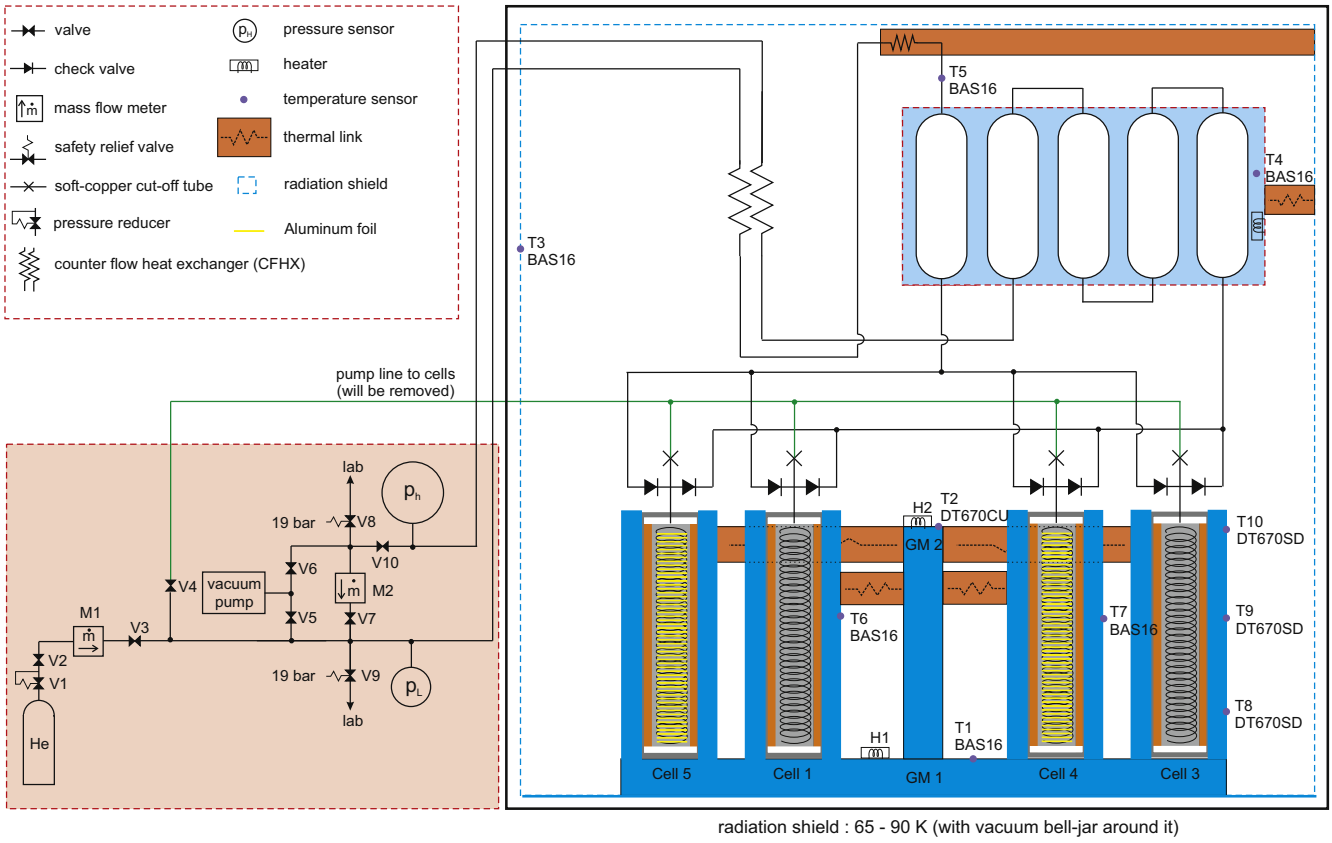

Fig. 2 – Schematic of the down-scaled helium sorption compressor setup for the METIS refrigerator.

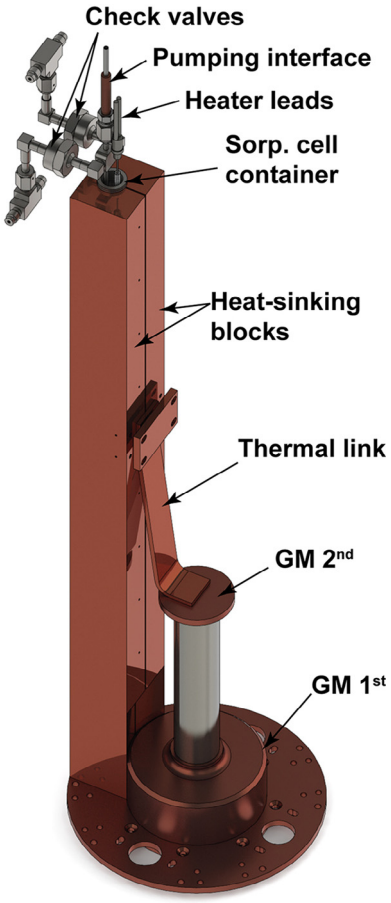

Fig. 3 – The heat-sink assembly: compressor cell clamped in copper blocks that is mounted on 1st GM stage plus separate link to 2nd stage.

as the 70 K radiation shield, are thermally attached to the 1st stage of the GM cooler.

The cold pressurized flow is warmed up to room temperature through a CFHX by the returning flow and then measured by the mass flow controller M2. The pressures at both sides of M2 are measured. The opening of M2 is controlled to maintain the average high pressure at a constant of 14.08 bar for the METIS helium refrigerator according to the optimized design presented in previous work (Wu et al., 2017c). For this purpose, the flow controller M2 is set by LabVIEW program to have a mass flow that is proportional to the measured high pressure p_h by introducing a scaling parameter C,

$$\dot{m} = Cp_h \tag{1}$$

At the start of the compressor operation, there is no pressure difference built up yet, and C is set to zero, i.e. the valve in M2 is fully closed. When the high pressure has reached a certain threshold level (e.g. 13.50 bar), C is set to an initial value C_{ini} that is based on the simulation results. Then, C is adjusted for each compression cycle, based on its value and the average high pressure measured in previous cycle,

$$C_i = C_{i-1}\frac{p_{h,avg,i-1}}{p_{h,setpoint}} \tag{2}$$

where i and i-1 indicate the current cycle and the previous cycle. In such way, if the average high pressure is higher than the desired setpoint value (in this case 14.08 bar), then the value of C in the control will be increased (the valve in the controller will open a bit more) to raise the flow rate, and vise versa. This iteration repeats until the average high pressure equals to P_h, setpoint. The low pressure should be 7.62 bar and is determined by M2 and V7, and by the filling pressure and the operating conditions of the system. Therefore, an additional mass flow meter M1 is used to record the mass that is filled into the system.

In order to have the temperature of the in-flow into the compressor cell at 70 K, an additional heat exchanger, with an effectiveness over 99.99% and pressure drop of 0.011 bar, is added between the low-pressure buffer and the CFHX. Soft copper pinch-off tubes connect the cells to the vacuum pump allowing to fill, pump and flush the cells before the experiment. After that, they are pinched and sealed, and the pumping line (green line) is removed.

Moreover, multiple temperature sensors were deployed to monitor the thermal behaviors of the setup, as shown in Fig. 2. Temperature sensor T1 and T2 were set for the 1st and 2nd stage of the GM cooler respectively; T3 was for measuring the radiation shield temperature; T4 was used for the buffers; and T5 was for monitoring the flow temperature at the high-pressure buffer inlet. T6 and T7 were mounted in the middle of Cells 1 and 4 at the positions of 272.5 mm from the bottom of the copper heat sink. T8, T9 and T10 were placed on Cell 3 at the positions of 122.5, 422.5 and 522.5 mm from the bottom of the copper heat sink, respectively.

Finally, the experimental setup was assembled, and Fig. 4 shows the cryogenic structure in the vacuum chamber before closing the radiation shield. Note that the buffer bottles are thermally mounted on the aluminum platform which is cooled

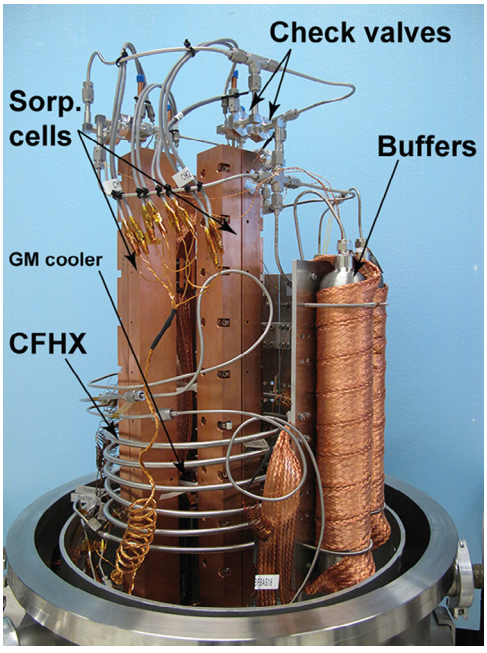

Fig. 4 – Experimental setup assembly in the vacuum chamber.

Table 1 – Detailed information about the major measuring sensors used in the experimental setup.

Sensor Symbol	Manufacturer	Model	Specification	Range	Accuracy
p_h	GE	PTX1400	–	25 bara	Combined non-linearity, hysteresis and repeatability: ± 0.15% typical, ±0.25% max. best straight line (BSL)
p_l	GE	UNIK5000	Industrial degree	25 barg	Combined non-linearity, hysteresis and repeatability: ± 0.2% FS BSL
M2	Bronkhorst	EL-FLOW	Calibrated by helium at 20 °C, 14.5 bara and 7.5 bara	10 ln/min	±(0.5% Rd + 0.1% FS)
T1, T3, T4, T5, T6, T7	Philips	BAS16	Diode in SOT23 package, 100 μA excited	300–50 K	±1.3 K (Rijpma and ter Brake, 2006)
T2	Lakeshore	DT670CU	Silicon diode in CU package, Standard curve Band A	500–1.4 K	From 2 K to 100 K: ± 0.25 K
T8, T9, T10	Lakeshore	DT670SD	Silicon diode in SD package, Standard curve Band A	500–1.4 K	From 2 K to 100 K: ± 0.25 K

by the 1st stage of the GM cooler. The CFHX surrounds the sorption-compressor cell tower, saving the limited space within the vacuum chamber.

Furthermore, detailed information about the major measuring sensor in the setup as shown in Fig. 2 is given in Table 1, including manufacturer, model, specification, range and accuracy of the sensor.

4. Experiment results and discussion

4.1. *Preparation and introductory test experiments*

The system was flushed with helium for several times first. Then the compressor cells were baked by the central heater with T6-T10 rising to 60 °C while the central temperature of the cells was about 100 °C. At the same time, the system was pumped down to 10^{-6} mbar. The baking process lasted for more than 24 h. After baking, the system was pre-charged to 5 bar, and a leak test was performed. The integral recording of M1 gave the total amount of helium that was filled into the system.

The system was first cooled down by the GM cooler with M2 and V7 fully open. Thus, the pressure in the system was uniform and, during the first 6.5 hrs of the cool-down process, it decreased gradually from the initial pre-charging pressure of 5.0 bar to 2.1 bar. Then, the cell temperatures (T6–T10) reached 80 K, and the system was further filled until the total amount of helium in the system reached the required level. The temperatures of the GM cold stages, T1 and T2 were controlled at 60 K and 50 K, respectively. It took another 9.5 hrs to cool the entire cold assembly to these temperatures.

In order to check the system operation, several introductory test experiments were performed. In these experiments, the heater of Cell 1 appeared not to function at the heat-sink temperature of 70 K although it worked fine at room temperature. We were not able to find the exact reason for this failure and to fix it. The most possible reason would be the thermal contraction due to the cryogenic temperature breaking the heater resistor or causing an internal electrical connection. Nevertheless, we were still able to run the other three cells with Cell 1 inactive as each compressor cell has its own check-valve unit.

Furthermore, the check valves were found not sealing very well due to the cryogenic temperature. Therefore, heaters and temperature sensors were placed on the check-valve units to keep them at a relatively high temperature (around 100 K). In addition, we kept a certain pressure difference between the check valves ($p_h > p_{cell} > p_l$) during the cool-down process and filling procedure to keep the sealing material in a proper shape at the operating temperature.

4.2. *Single-cell experimental results*

A default setting of each cell was chosen according to the simulation results of the sorption compressor model: pulsed heating power for each cell was 150 W; heating time was 8.73 s; cycle time was 103.6 s; average heat-sink temperature was 70 K; and high pressure was 14.08 bar. Although the buffer volumes were used in the system to dampen the pressure swing, there is still significant pressure oscillation along the cycling period, especially for single-cell operation. As explained in Sec. 3, M2 controls the mass flow in proportion to the average high pressure ($\dot{m} = Cp_h$). In the case of single-cell operation, the average is taken over each single full cycle. The value of C is stepwise changed until the measured average pressure equals 14.08 bar. In this process, the ratio of the new value of C to its old value equals the ratio of the measured average high pressure to the desired value (i.e. 14.08 bar). So, if the pressure is a factor of two too high, then C should be increased by that factor of 2. After a few cycles, the average pressure is 14.08 bar and the value of C at that point gives the corresponding mass flow rate.

The performance of the individual cells operating at nominal conditions was tested. In Fig. 5, the plots on the left present the pressure, mass flow rates (raw and filtered) and temperature measurements of Cell 3 operating at nominal conditions. The pressure swings in high and low pressures were about 0.4 bar. These pressure swings influence the performance of the sorption compressor since they allow the cell to produce an out-flow at relatively higher pressure and to adsorb an in-flow at relatively lower pressure. As explained above, the average high pressure was controlled at 14.08 bar. The measured average low pressure was 7.48 (7.48 ± 0.05) bar, slightly lower than the design value. As a result of the dynamic control in M2, the mass flow showed significant high-frequency noise. This was filtered by a Savitzky–Golay filter ($k = 3$, $f = 399$, k is the polynomial order and f is the frame size), resulting in a flow fluctuation of less than 15%. At the high pressure of 14.08 bar, Cell 3 established an average mass flow rate of 2.73 (2.73 ± 0.05) mg s^{-1}.

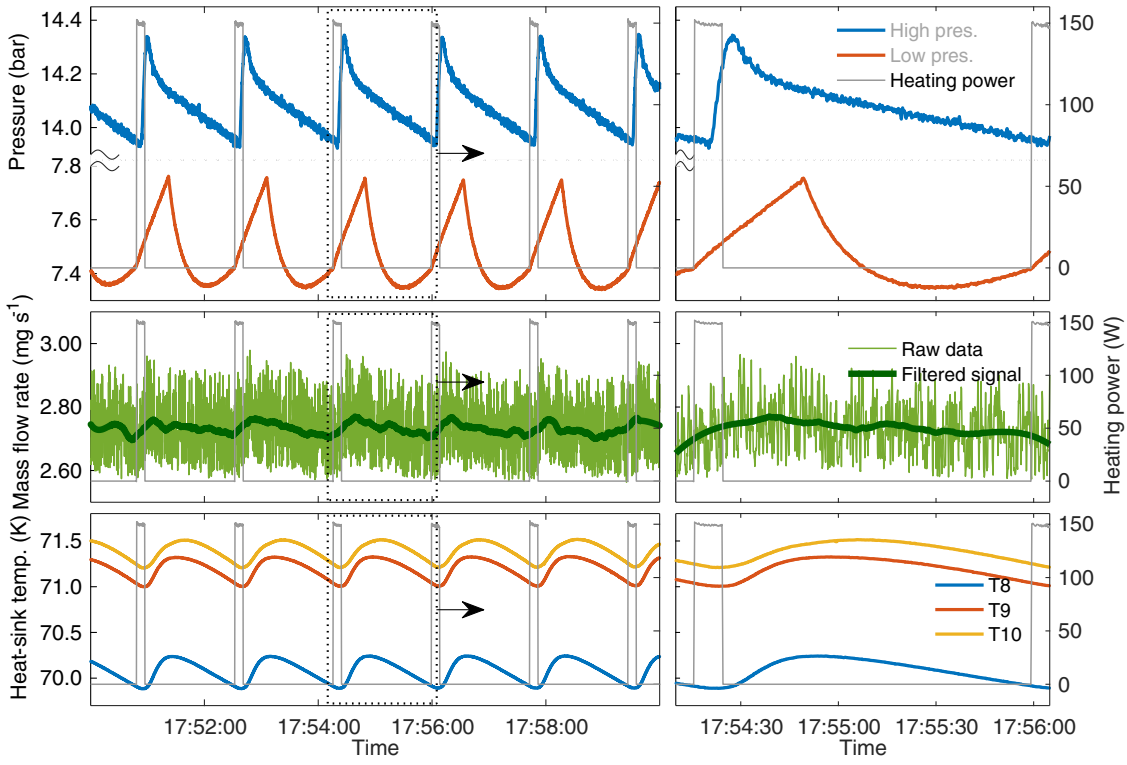

Fig. 5 – Pressures, mass flow rates (raw and filtered by a Savitzky–Golay filter ($k = 3$, $f = 399$)), temperatures and heating powers measurements for Cell 3 operating at default setting. Left: a few cycles in stable operation; Right: one cycle enlarged.

The heat-sink temperature oscillated about 0.3 K due to the periodic heating. According to T8, T9, T10 and the cooling temperatures of the GM cooler T1 and T2, the average heat-sink temperature of the copper heat-sink blocks is 70.6 (70.6 ± 0.5) K. And the maximum temperature deviation of the heat-sink temperature is about 0.9 K which is very close to the estimation of 1.05 K as mentioned in Sec.3.

The right plots in Fig. 5 zoom in on one particular cycle. In the heating period, the high pressure did not rise until the pressure in the cell was built up in about 4 s. Then the high-pressure check valve opened and the high pressure increased rapidly. Meanwhile, the low pressure rose linearly because of the mass flow from high-pressure side to the low-pressure side. When the heating stopped, the high-pressure check valve closed in about 3.5 s. Then the high pressure started to decrease because, firstly, the flow continued out of the high-pressure buffer and, secondly, the pressurized hot fluid was cooled down in the high-pressure buffer. It took another 20 s to reduce the pressure inside the cell to below the level of the low-pressure buffer. Then the low-pressure check valve opened and allowed the fluid to flow into the cell resulting in a reduction of the pressure in the low-pressure buffer. The low pressure went up at the end of the cycle as the in-flow of the cell becomes smaller than the flow through M2.

Thermal improvement by inserting aluminum foil between the carbon pills for increasing the effective radial conductivity was proposed by our previous work (Mulder, 2014). The radial conductance enhanced cell was expected to achieve 24% higher flow rate with 21% additional input power based on simulations in which the cycle is controlled on the basis of temperatures. However, the compression cycles were controlled by time in the practice. Therefore, we were able to primarily verify the improved concept comparing the baseline design with the same input power. Fig. 6 shows the comparison between the performance of the baseline cell (Cell 3) and that of the radial-conductance-enhanced cells (Cells 4 and 5). The Cells 4 and 5 generated higher mass flows than Cell 3 by a factor of 8.7% and 7.2%, respectively. By examining the pressures measured in the experiment shown in Fig. 7, in Cell 4, the high pressure started to rise earlier and had a higher peak than that in Cell 3. Thus, the pressure was built up faster in the compression

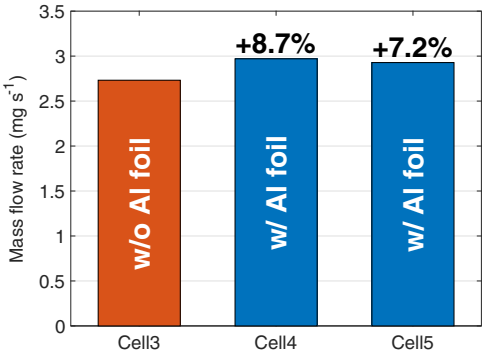

Fig. 6 – Measured average mass flow rate comparison between Cells 3, 4 and 5.

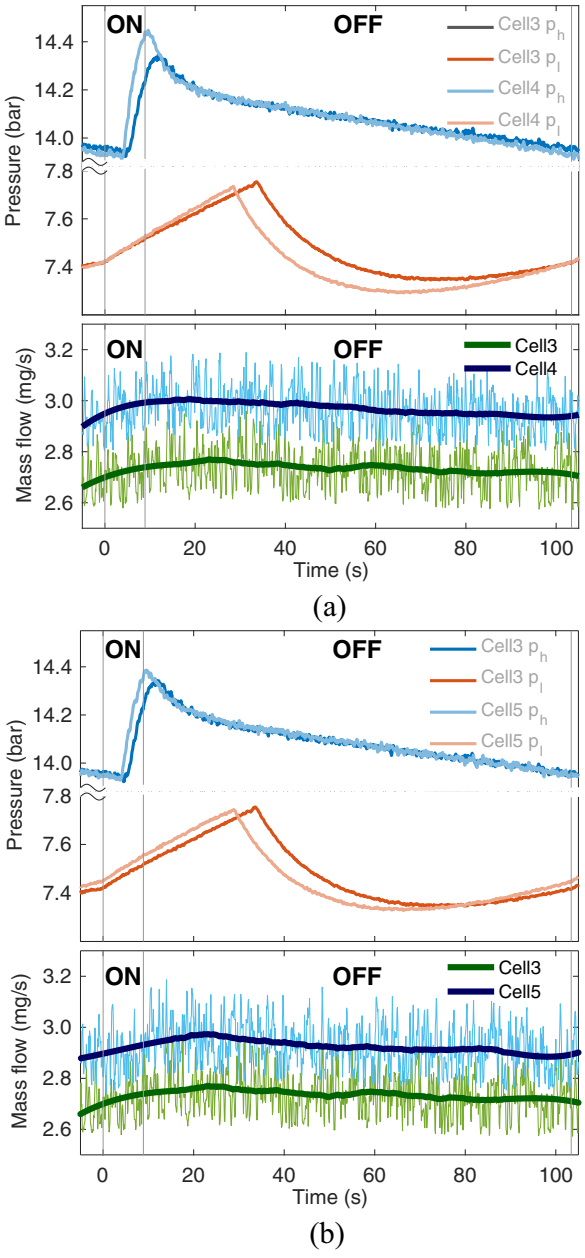

Fig. 7 – Measured pressures and mass flow rates comparison between (a) Cells 3 and 4; (b) Cells 3 and 5 in a particular cycle.

phase, and a higher out-flow rate was obtained. The out-flow phase period seemed to be shortened in Cell 4 as well as in the subsequent decompression phase (low pressure dropped earlier) thanks to the radial-enhanced conductance causing a faster thermal cycling. Due to the higher radial conductance,

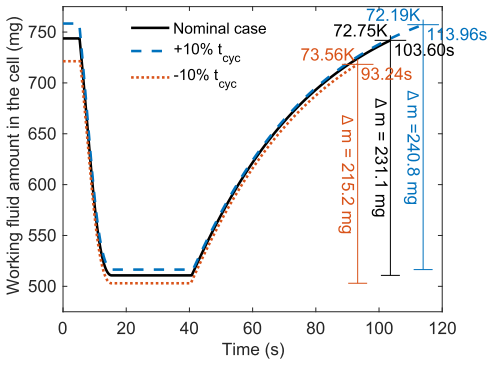

Fig. 8 – Simulated fluid amount in the cell during the cycle for different cycle time.

the thermal conduction loss to the heat sink during the heating period also increases. However, the heating time of the nominal setting was short (8.73 s) to minimize these conduction losses. The negative effect of these increased conduction losses is relatively small compared to the benefit of faster thermal cycling.

4.3. *Performance sensitivity*

Increasing the operating frequency, or rotational speed of a rotary compressor compared to its optimum setting,will increase its capacity but at the same time degrade its efficiency (Radebaugh and O'Gallagher, 2006; Radebaugh, 2007). The same applies to a sorption compressor although it operates at a very low frequency compared to the 50–60 Hz that is usually found in mechanical compressors. Changing the sorption compressor frequency was tested by varying the cycling time. Here, the compressor efficiency is defined by the ratio of the mass flow rate and the average input power since the pressures and the heat-sink temperature are all the same in all cases. Table 2 lists the performance of Cell 3 at different cycle time settings. Cases 29 and 30 are operating at –10% and +10% cycle time, respectively compared to Case 27 which shows the performance at default setting. With the same heating energy, the average input powers were +11.1% and –9.9% for Cases 29 and 30, respectively. At faster cycling (Case 29), the compressor capacity, i.e. the mass flow rate, was improved by 5.9% but the corresponding efficiency degraded by 4.6%. Cycling slower (Case 30) yields a higher efficiency (+2.3%) but generates less mass flow (–6.6%) which means that more cells are required for a specific refrigeration capacity. Numerical simulation was performed to investigate the details of the cell operation with changing cycle time. Fig. 8 presents the simulated amount of working fluid in the cell as a function of time. The minimum amounts when the cell is at its highest temperature are not too much different as the cycle time changes. However, the slower cycling case

Table 2 – Sorption compressor performance within different cycle time (Cell 3).

Case	Description	P_{HT}, W	t_H, s	t_{cyc}, s	P_{avg}, W	$\dot{m}$	Eff., mg J^{-1}
27	default setting	150	8.73	103.60	12.64	2.73	0.216
29	–10% t_{cyc}	150	8.73	93.24	$14.04^{+11.1\%}$	$2.89^{+5.9\%}$	$0.206^{-4.6\%}$
30	+10% t_{cyc}	150	8.73	113.96	$11.49^{-9.9\%}$	$2.55^{-6.6\%}$	$0.221^{+2.3\%}$

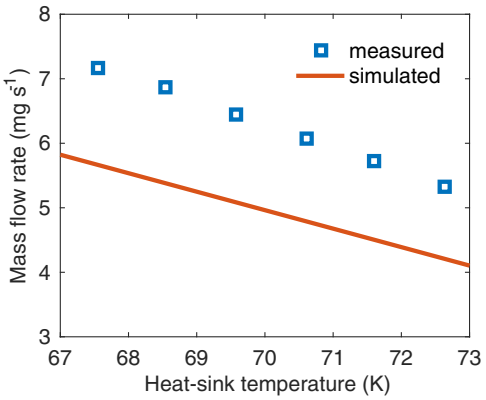

Fig. 9 – Mass flow rate generated by the sorption compressor as a function of the heat-sink temperature.

having 10 s more cooling down time allows the carbon being cooled down from 72.75 K to 72.19 K (average temperature) thus adsorbing 4.20% more of the working fluid. Similarly, the adsorption is 15.9 mg (6.88%) less and average low temperature of the carbon is 0.8 K higher in the faster cycling case. Therefore, the lower efficiency at faster cycling is because there is not sufficient time for full adsorption during the in-flow phase.

As mentioned in the baseline design of the METIS refrigerator (Wu et al., 2017c), the heat-sink temperature of the sorption compressor determines the low-temperature level of the sorption compressor cycle and thus strongly influences the compressor performance. Such statement has been experimentally proven in current study. Cell 3 and 4, cycling out of phase, were operated at various heat-sink temperatures from 67 K to 72 K while the other settings were kept the same. As shown in Fig. 9, the measured average mass flow rate was significantly improved by decreasing the heat-sink temperature, and the sensitivity of the sorption compressor efficiency with respect to the heatsink temperature at 70 K is 5.75% per kelvin. Fig. 9 also presents the simulated performance (Cell 3 + Cell 4) and shows very similar tendency and sensitivity in the range of 67–72 K as the experimental results although the calculated mass flow rate is roughly 21% lower than the measured values.

4.4. *Multi-cells operation*

Cells 3, 4 and 5 were cycled together with 120° phase difference. The stable operation status is plotted in Fig. 10. The pressures oscillated 3 times faster than in the single-cell case. The amplitude of the high-pressure oscillation did not reduce because the out-flow period is very short, i.e. 10% of the total cycle. In order to reduce the high-pressure swing more than 10 cells would be needed. In that case, the out-flow periods of the cells would overlap. The low-pressure swing, however, was reduced since the in-flow period of the cells is almost half of the cycle and thus significantly overlaps when three cells are used. The faster variation of the high pressure at equal amplitudes resulted in a larger instability of the flow rate (as a

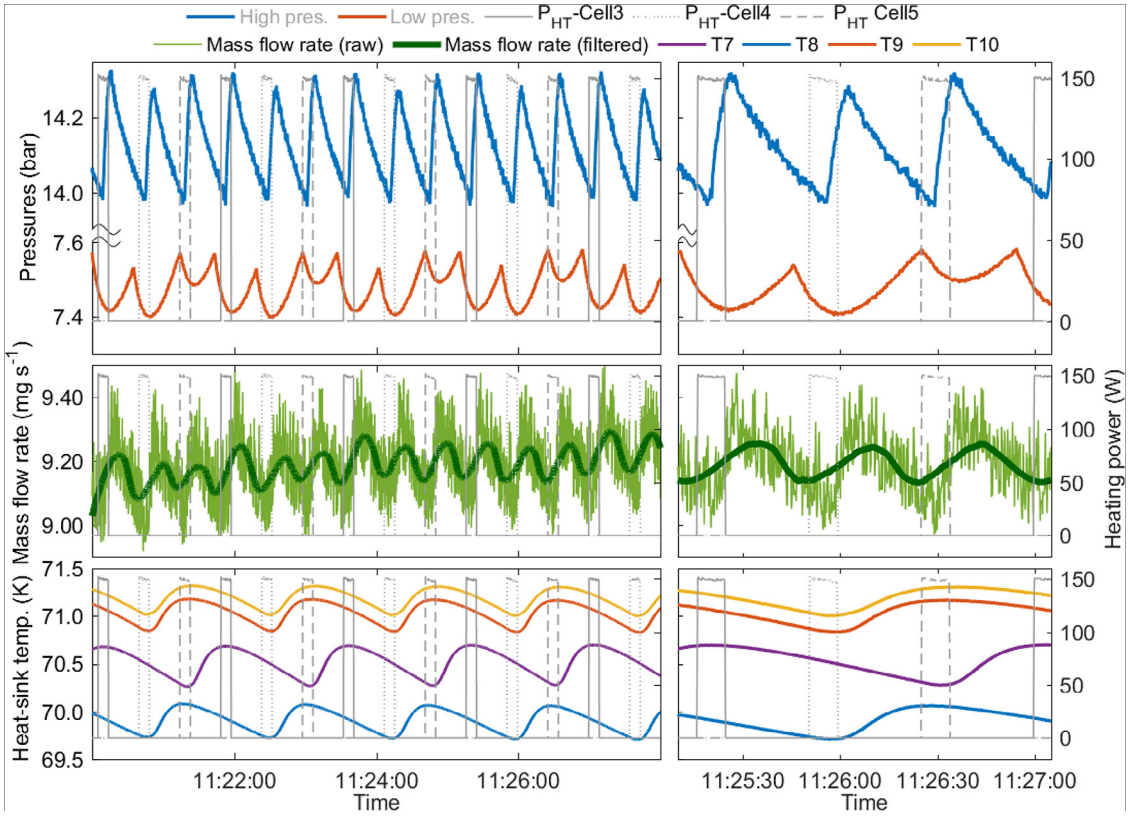

Fig. 10 – Pressures, mass flow rate, temperatures and heating powers measurements for Cell 3, 4 and 5 operating in parallel at the nominal condition. Left: stable operations; Right: measurement of one particular cycle.

result of the operation of mass-flow controller M2 as discussed above). With an average heat-sink temperature of 70.4 (70.4 ± 0.5) K, a total average flow rate of 9.19 (9.19 ± 0.08) mg s^{-1} was achieved. In the multi-cell operation, the oscillation at the low-pressure side is reduced compared to the single-cell operation. Therefore, the total flow rate is higher than the sum of the flow rates that were measured in the single-cell operation.

4.5. *Comparison between the single-cell experiment results and simulations*

Operating parameters such as pressures, average heat-sink temperature, heating power, timing and compressor-cell dimensions were input into the one-dimensional dynamic model (Wu et al., 2017a) for simulating the performance of the baseline cell. The simulation shows that the baseline cell can generate 2.25 mg s^{-1} at default setting, which is 17.7% less than the measured value (2.73 mg s^{-1}). Further relating the experimental results to simulations, the duration of each phase in compression cycle are compared in Table 3. The measured compression (5.50 s vs. 5.23 s) and in-flow (70.10 s vs. 65.89 s) times are close to the simulated value. Since the in-flow phase timing is more or less determined by the cycle time, there is a relatively small difference between the experiment and the simulation. However, the measured out-flow stopped 3.71 s earlier and the actual out-flow duration is 36.34% less compared to the simulation. This may be partly because of the fact that in the simulations the high pressure is considered to be constant, whereas in reality, due to the heat pulse and mass flow controlling mechanism, the high pressure rapidly increases and has a peak during the compression phase, as shown in Fig. 11. However, the experiment cell pumped more working fluid to even higher pressure within shorter time. The total desorption time for the cell is 12 s compared to 15.44 s in the simulation, indicating that the desorption/adsorption loop is stronger than expected.

The underestimated simulated results can be caused by a number of reasons:

Underestimation of the adsorption capacity of the carbon: The isotherm measurement normally has an uncertainty of 5–15%. Therefore, it is possible that the saran carbon that we used has a larger difference in adsorption amount between the low-temperature, low-pressure state and the high-temperature, high-pressure state than that assumed in the simulations. The simulated performance of the sorption cell is directly related to the isotherm data. To investigate the influence from the inaccuracy of the isotherm data, a scaling factor was applied in the calculation of the adsorbed amount to simulate a deviation of the actual adsorption with respect to the calculated one. Fig. 12 presents the mass flow rate per cell as a function of this scaling factor. The performance (mass flow rate per cell) increases almost linearly as the scaling factor increases up to 1.25. The sensitivity is about 0.0135 (mg s^{-1})/% (or 0.60 %/%).

Overestimation of the heat capacity of the adsorption mixture: In the helium sorption compressor operation, the heat capacity of the saran carbon (<70%) and that of the helium in the adsorbed phase (20–30%) dominate the total heat capacity of the adsorption mixture. If these are overestimated in the simulation, the adsorption mixture would be cycled in a lower temperature difference resulting in a lower efficiency. In order to evaluate this effect, we simulated the performance with reduced heat capacity of the carbon and the adsorbed helium again by introducing a scaling factor. As shown in Fig. 13, the sensitivity is about –0.0149 (mg s^{-1})/% (or 0.66 %/%).

Underestimation of the effective thermal conductivity of the adsorption mixture: A higher thermal conductance in the adsorption mixture would result in a more evenly distributed temperature and would make the utilization of the adsorbent material more efficient. Consequently, it would improve the performance of the sorption-compressor cell. Therefore, if the effective thermal conductivity of the adsorption mixture was underestimated in the model, the simulation

Table 3 – Comparison between the measured and simulated periods of four phases in a sorption compression cycle (Cell 3).

Time (s)	Measured (Cell 3)	Simulated
Compression	5.50 (+5.16%)	5.23
Out-flow	6.50 (–36.34%)	10.21
Decompression	21.5 (–14.92%)	25.27
In-flow	70.10 (+6.39%)	65.89

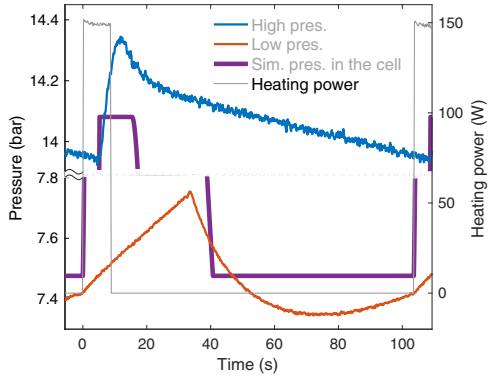

Fig. 11 – Simulated pressure in the cell compared to the measured pressures for single-cell operation (Cell 3, default setting).

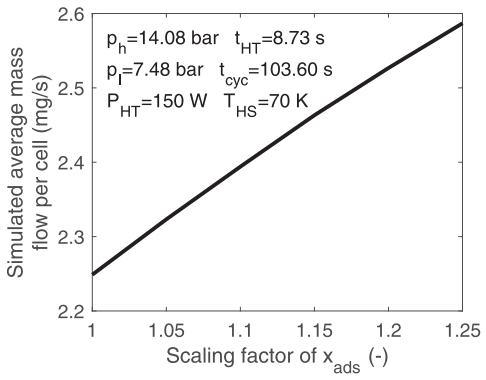

Fig. 12 – Simulated average mass flow rate per cell as a function of the adsorption amount scaling factor.

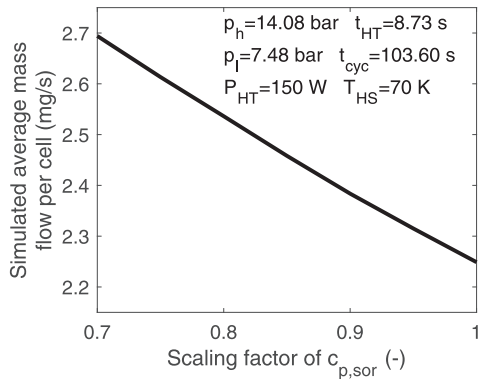

Fig. 13 – Simulated mass flow rate per cell as a function of the heat-capacity scaling factor.

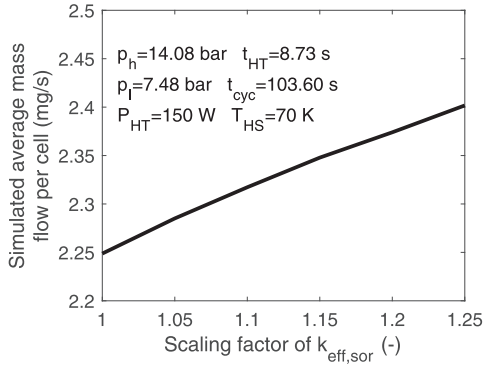

Fig. 14 – Simulated average mass flow rate per cell as a function of an effective thermal conductivity scaling factor of the adsorbent mixture.

would naturally give a lower performance than expected. Fig. 14 presents the simulated average mass flow rate per cell as a function of an effective thermal conductivity scaling factor that was applied to the adsorption mixture. Note that this effect is not as strong as the previous two effects (0.27 %/%, or 0.0061 (mg s^{-1})/%).

Neglecting the fluid dynamics in the cell during the out-flow phase: A significant difference between the experiment and simulation occurs in the out-flow phase as the peak out-flow may cause complicated fluid dynamics in the cell that may not be negligible. The convection effect of the fluid in the out-flow phase may be beneficial in distributing the temperature more evenly and thus improving the performance. Nevertheless, the evaluation of the convection effect requires a multi-dimensional model that includes the fluid dynamics, which is not available now and out of the scope of this paper. Such dynamic effect shall be further investigated in the future.

Nevertheless, the 1-D dynamic model is able to simulate the sorption-compressor cell operation well, and predict the sorption-compressor cell performance within a reasonable accuracy. Deviations between simulation and experimental results are measured to be about 17–20% and can be accounted for by inaccuracies in model input parameters such as isotherm data, specific heat, and thermal conductivity. Despite the sensitivity to these input parameters, the model is very useful for design purposes. Furthermore, the better experimental performance of the sorption-compressor cells also indicates that the required cell number can be reduced by about 15–17% than estimated in the theoretical design phase.

5. Conclusion

A down-scaled helium sorption compressor for the METIS refrigerator was designed, fabricated, assembled and tested. It consists of four compressor cells connected in parallel with individual check valves. Two cells are made following the baseline cell design, one cell of which, unfortunately, could not be used because of a heater defect. The other two cells have an enhanced radial conduction by inserting aluminum foil between the carbon pills. The baseline cell can produce a mass flow rate of 2.73 mg s^{-1} between 14.08 bar and 7.48 bar with a heat-sink temperature of 70 K. The improvement by increasing the effective conductivity of the adsorbent material was verified: the other two cells performed better in the same setting by a factor of 8.7% and 7.2%.

The sorption compressor performance against the cycling time and the heat-sink temperature was also investigated. As the cycle time is increased, the cell can cool down closer to the heat-sink temperature and thus more gas is adsorbed. As a result, the efficiency increases but because of the longer cycle time, the average mass flow rate decreases. Thus, a trade-off can be made between efficiency and number of cells needed for a specific refrigeration power. The heat-sink temperature has a strong effect. The efficiency changes close to 6% per kelvin of change in heat-sink temperature.

Finally, the compressor was operated with three cells running 120° out of phase, and a total mass flow rate of 9.2 mg s^{-1} was achieved. Furthermore, the 1-D dynamic model described in previous work appears to simulate the compressor operation very well. Deviations between simulation and experimental results are measured to be about a few percent and can fully be accounted for by inaccuracies in model input parameters such as isotherm data, specific heat, and thermal conductivity. Despite the sensitivity to these input parameters, the model is very useful for design purposes. According to the better experimental performance of the sorption-compressor cell, the required cell number for METIS refrigerator can be reduced by about 15–17% than estimated in the theoretical design phase.

Acknowledgments

This research is enabled through the Netherlands Research School for Astronomy (NOVA) by financial support from the Netherlands Organisation for Scientific Research (NWO) under contract 184.021.006.

REFERENCES

Brandl, B.R., Lenzen, R., Pantin, E., Glasse, A., Blommaert, J., Venema, L., et al., 2010. Instrument concept and science case

for the mid-IR E-ELT imager and spectrograph METIS. In: McLean, I.S., Ramsay, S.K., Takami, H. (Eds.), Ground-based and Airborne Instrumentation for Astronomy III. p. 77352G. Proc. SPIE 7735.

Burger, J.F., ter Brake, H.J.M., Holland, H.J., Meijer, R.J., Veenstra, T.T., Venhorst, G.C.F., et al., 2007. Long-life vibration-free 4.5 K sorption cooler for space applications. Rev. Sci. Instrum. 78, 65102–65110.

Marquardt, E.D., Le, J.P., Radebaugh, R., 2001. Cryogenic material properties database. In: Ross, R.G.J. (Ed.), Cryocoolers 11. Kluwer Acadamic / Plunum Publishers, New York, US, pp. 681–687.

Mulder, T., 2014. New sorption compressor designs for the METIS cooler in the E-ELT. (Master's thesis). University of Twente. Enschede, The Netherlands.

Radebaugh, R., 2007. Packing more power in a small volume. Cold Facts 23, 19–27.

Radebaugh, R., O'Gallagher, A., 2006. Regenerator operation at very high frequency for microcoolers. In: Weisend, J.G., II (Ed.), Advances in Cryogenic Engineering 51B. American Institute of Physics, Melville, New York., pp. 1919–1928.

Rijpma, A.P., ter Brake, H.J.M., 2006. Cryogenic thermometry with a common diode: type BAS16. Cryogenics 46, 68–69.

Wiegerinck, G.F.M., Burger, J.F., Holland, H.J., Hondebrink, E., ter Brake, H.J.M., Rogalla, H., 2006. A sorption compressor with a single sorber bed for use with a Linde-Hampson cold stage. Cryogenics 46, 9–20.

Wu, Y., Mulder, T., Vermeer, C.H., Holland, H.J., ter Brake, H.J.M., 2017a. A 1-dimensional dynamic model for a sorption-compressor cell. Int. J. Heat Mass Transf. 107, 213–224.

Wu, Y., Vermeer, C., Holland, H.J., ter Brake, H.J.M., 2017b. Development of a switchless sorption compressor for the cryogenic refrigeration within the METIS instruments: part I. Theoretical design. Int. J. Refrigeration.

Wu, Y., Zalewski, D., Vermeer, C., Holland, H.J., Benthem, B., ter Brake, H.J.M., 2017c. Baseline design of a sorption-based Joule-Thomson cooler chain for the METIS instrument in E-ELT. Cryogenics 84, 37–52.